



Cite as

Nano-Micro Lett.
(2023) 15:189

Received: 5 May 2023
Accepted: 19 June 2023
Published online: 29 July 2023
© The Author(s) 2023

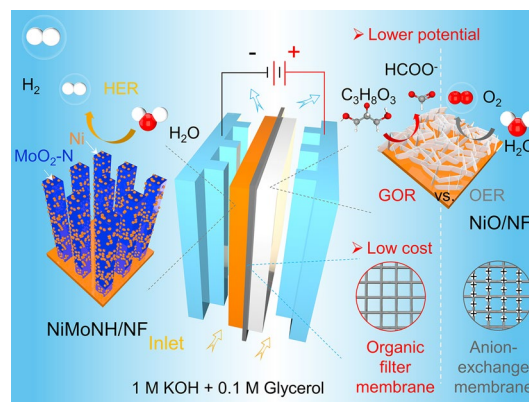
Vertical 3D Nanostructures Boost Efficient Hydrogen Production Coupled with Glycerol Oxidation Under Alkaline Conditions

Shanlin Li^{1,2}, Danmin Liu¹ ✉, Guowei Wang¹, Peijie Ma¹, Xunlu Wang²,
Jiacheng Wang^{2,4,5} ✉, Ruguang Ma³ ✉

HIGHLIGHTS

- Two types of vertical 3D nanostructures were successfully fabricated using simple hydrothermal and heat treatment processes for hydrogen evolution reaction and glycerol oxidation reaction (GOR).
- Hydrogen production at a lower potential was achieved by replacing oxygen evolution reaction with GOR, reducing the device potential by approximately 300 mV. Additionally, organic membranes were used as separators, avoiding the use of expensive anion exchange membranes.

ABSTRACT Hydrogen production from electrolytic water is an important sustainable technology to realize renewable energy conversion and carbon neutrality. However, it is limited by the high overpotential of oxygen evolution reaction (OER) at the anode. To reduce the operating voltage of electrolyzer, herein thermodynamically favorable glycerol oxidation reaction (GOR) is proposed to replace the OER. Moreover, vertical NiO flakes and NiMoNH nanopillars are developed to boost the reaction kinetics of anodic GOR and cathodic hydrogen evolution, respectively. Meanwhile, excluding the explosion risk of mixed H₂/O₂, a cheap organic membrane is used to replace the expensive anion exchange membrane in the electrolyzer. Impressively, the electrolyzer delivers a remarkable reduction of operation voltage by 280 mV, and exhibits good long-term stability. This work provides a new paradigm of hydrogen production with low cost and good feasibility.



KEYWORDS Hydrogen evolution reaction; Glycerol oxidation reaction; Oxygen evolution reaction; Flow cell; Nanostructure

✉ Danmin Liu, dmliu@bjut.edu.cn; Jiacheng Wang, jiacheng.wang@mail.sic.ac.cn; Ruguang Ma, ruguangma@usts.edu.cn
¹ Key Laboratory of Advanced Functional Materials, Ministry of Education, Faculty of Materials and Manufacturing, Beijing University of Technology, Beijing 100124, People's Republic of China

² The State Key Laboratory of High Performance Ceramics and Superfine Microstructure, Shanghai Institute of Ceramics, Chinese Academy of Sciences, Shanghai 200050, People's Republic of China

³ School of Materials Science and Engineering, Suzhou University of Science and Technology, 99 Xuefu Road, Suzhou 215011, People's Republic of China

⁴ School of Materials Science and Engineering, Taizhou University, Taizhou 318000, People's Republic of China

⁵ Hebei Provincial Key Laboratory of Inorganic Nonmetallic Materials, College of Materials Science and Engineering, North China University of Science and Technology, Tangshan 063210, People's Republic of China


1 Introduction

Water electrolysis technology is promising to convert clean electricity generated by intermittent wind and solar energy into storable green hydrogen energy, which is one of the important paths to achieve carbon neutrality [1–4]. The electrolytic water process usually consists of two half-reactions, the anodic oxygen evolution reaction (OER) and the cathodic hydrogen evolution reaction (HER). However, the anodic four-electron OER with slow kinetics and high overpotential is the key limitation of the water splitting [5–7]. A great deal of studies in the past have focused on the design and development of advanced OER electrocatalysts to reduce the power consumption and cost of hydrogen production from electrolytic water. However, the anodic product oxygen (O_2) is usually a worthless and energy-consuming by-product accompanying hydrogen production from electrolytic water. In addition, the generated gas products may form hazardous H_2/O_2 mixture, which require additionally costly proton exchange membrane (PEM, $\$4.2\text{ kg}^{-1}$) or anion-exchange membrane (AEM, $\$3.7\text{ kg}^{-1}$) [8] to separate the cathode and anode chambers. Furthermore, the generated reactive oxygen species (ROS) will shorten the lifetime of the membrane [9, 10]. In a word, the high energy consumption and the safety issues had limited the development of electrolytic water.

Recently, a number of thermodynamically and economically favorable oxidation reactions have been widely explored to replace the sluggish OER, which were coupled with the HER for H_2 production [6, 7, 11]. Among these alternative reactions, one type is the oxidation of sacrificial agents, such as hydrazine oxidation reaction (HzOR, $N_2H_4 + 4OH^- \rightarrow N_2 + 4H_2O + 4e^-$, -0.33 V vs. RHE) [12, 13], urea oxidation reaction (UOR, $CO(NH_2)_2 + 6OH^- \rightarrow N_2 + CO_2 + 5H_2O + 6e^-$, 0.37 V vs. RHE) [14, 15], whose products are N_2 and other safe gases. Another one is the organic upgrading reaction, which can significantly reduce the anode potential and obtain high value-added chemicals at the same time, such as methanol oxidation reaction (MOR, $CH_3OH + 5OH^- \rightarrow HCOO^- + 4H_2O + 4e^-$) [16–19], glycerol oxidation reaction (GOR, $C_3H_8O_3 + 8OH^- \rightarrow 3HCOOH + 5H_2O + 8e^-$, 0.69 V vs. SHE) [20, 21], 5-hydroxymethyl furfural (HMF) oxidation [22, 23], aldehydes oxidation [8, 24], glucose oxidation [25, 26]. It is noted that coupling HER with the oxidation

reaction of organic molecules can achieve the acquisition of H_2 and high value-added organic molecules at low potentials. Glycerol is a low-value byproduct of biodiesel production [27], while its oxidation product formate ($HCOO^-$) or formic acid ($HCOOH$) is widely used in industrial production [20]. Unfortunately, it is still highly in demand on low-cost and highly active catalysts for glycerol oxidation.

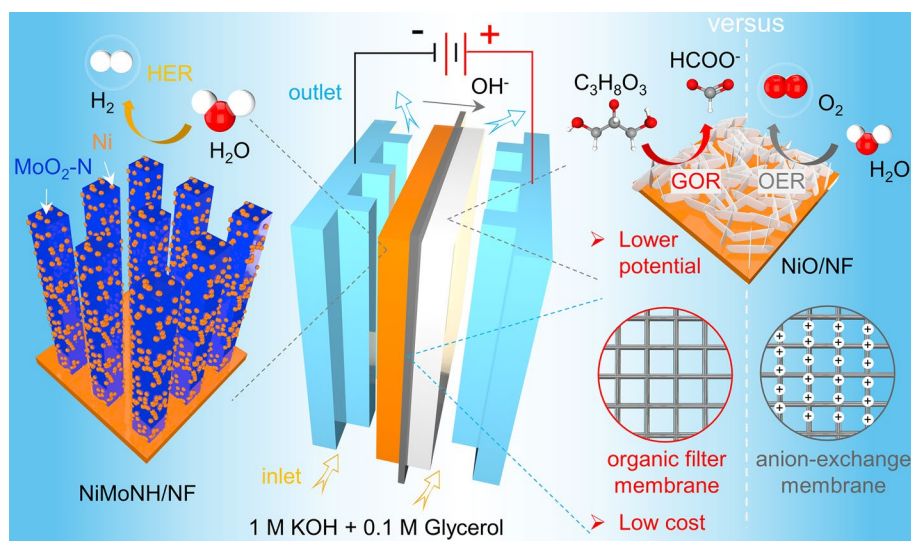
In this work, we develop a hybrid water electrolysis flow cell for hydrogen production coupled to glycerol oxidation based on a nickel-based catalyst and using inexpensive organic membranes (Scheme 1). Specifically, for the anodic glycerol oxidation reaction (GOR), we used nickel oxide (NiO) nanosheet arrays as an electrocatalyst, which exhibited better activity than nickel hydroxide ($Ni(OH)_2$). The addition of glycerol molecules significantly reduces the anodic potential compared to the conventional OER. At the cathode, we used NiMoNH nanopillar arrays as a HER electrocatalyst, which were obtained by annealing NiMoO in ammonia (NH_3) and argon–hydrogen (Ar/H_2) mixture gas. The addition of glycerol molecules remarkably decreases the voltage of electrolyze, which is beneficial for the reduction of energy consumption. Moreover, the alkaline anion exchange membrane can be replaced with an inexpensive organic filter membrane, without degradation of electrochemical performance. This study opens up a new point of view for the future exploration of practical hybrid water electrolyzer.

2 Experimental Section

2.1 Preparation of Catalysts

2.1.1 Synthesis of $Ni(OH)_2$

A piece of nickel foam (NF) ($3\text{ cm} \times 6\text{ cm}$) was first cleaned by sonicating in 0.1 M HCl, deionized water, and ethanol for 15 min each. Then, 1.45 g nickel (II) nitrate hexahydrate ($Ni(NO_3)_2 \cdot 6H_2O$) and 1.4 g hexamethylenetetramine (HMT) were dissolved in 70 mL deionized water and stirred for 30 min. This solution was then poured into a Teflon-lined stainless steel autoclave, and then the cleaning NF was immersed in it before being heated to $120\text{ }^\circ\text{C}$ for 6 h. After cooling down to room temperature, the resulting $Ni(OH)_2$



Scheme 1 Design of the hybrid water electrolyser

nanosheets on the NF were rinsed with deionized water and left to dry naturally.

2.1.2 Synthesis of NiO

The as-grown $\text{Ni}(\text{OH})_2$ precursor was heated in a quartz tube furnace at 300 °C for 3 h under air to convert into NiO.

2.1.3 Synthesis of NiMoO

1.4 g $\text{Ni}(\text{NO}_3)_2 \cdot 6\text{H}_2\text{O}$ and 1.48 g ammonium molybdate tetrahydrate ($(\text{NH}_4)_6\text{Mo}_7\text{O}_{24} \cdot 4\text{H}_2\text{O}$) were dissolved in 80 mL deionized water and stirred for 30 min. Then, this solution was transferred to a Teflon-lined stainless steel autoclave, and then immersed the NF into the solution and heated to 150 °C for 6 h. After cooling down to room temperature, the obtained NiMoO supported on NF were washed with deionized water and then dried naturally.

2.1.4 Synthesis of NiMoNH

The as-grown NiMoO precursor on the NF was annealed in a quartz tube furnace at 400 °C for 2 h in an NH_3 atmosphere

to turn it into NiMoN. The NiMoN was then heated in a quartz tube furnace at 500 °C for 2 h in an Ar/H_2 atmosphere to form NiMoNH.

2.2 Characterization

2.2.1 Materials Characterization

A field emission scanning electron microscope (FEI Magellan 400L XHR) was used for obtaining the scanning electron microscopy (SEM) images. A Titan G2 60–300 Cs-corrected transmission electron microscopy (TEM) was used for TEM, high-resolution TEM (HRTEM), high angle annular dark-field scanning TEM (HAADF-STEM), and energy-dispersive X-ray spectroscopy (EDS) mapping. X-ray diffraction (XRD) measurements were performed on a Bruker D8 ADVANCE X-ray diffraction diffractometer. A Thermo ESCALAB250xi electron spectrometer with an $\text{Al K}\alpha$ source (1486.6 eV) as radiation source was used for X-ray photoelectron spectroscopy (XPS) measurements. A Bruker A300 spectrometer was used for acquiring the Electron Paramagnetic Resonance (EPR) spectra.



2.2.2 Electrochemical Characterization

We used a CHI 760E electrochemical workstation to perform electrochemical measurements in an H-type three-electrode cell (H cell). A graphite rod electrode and a Hg/HgO were used as the counter electrode and reference electrode, respectively. The working electrode (1 cm × 1 cm) was using the as-prepared self-supporting electrodes. Fumasep FAB-PK-130 was used as the anion exchange membrane (AEM). All the potentials versus Hg/HgO were converted to the values versus the reversible hydrogen electrode (RHE) using the equation: $E \text{ vs. RHE} = E \text{ versus Hg/HgO} + 0.924 \text{ V}$.

We prepared a membrane electrode assembly (MEA) for testing the electrochemical performance in a flow cell (Gaosunion Co., Ltd., Tianjin, China). The MEA was made by

sandwiching NiO and NiMoNH electrode between either a commercial membrane (Fumasep FAB-PK-130) or an organic membrane. The MEA was then placed within a custom-designed electrolyzer where 1 M KOH and 0.1 M glycerol were circulated through cathode and anode as the electrolyte.

3 Results and Discussion

3.1 Characterization of NiO and Ni(OH)₂

Figure S1 shows the synthesis of NiO catalyst. A commercially available nickel foam (NF) was used as the conductive substrate. Firstly, the nickel hydroxide (Ni(OH)₂) precursor grew on the NF through a hydrothermal reaction of nitrate

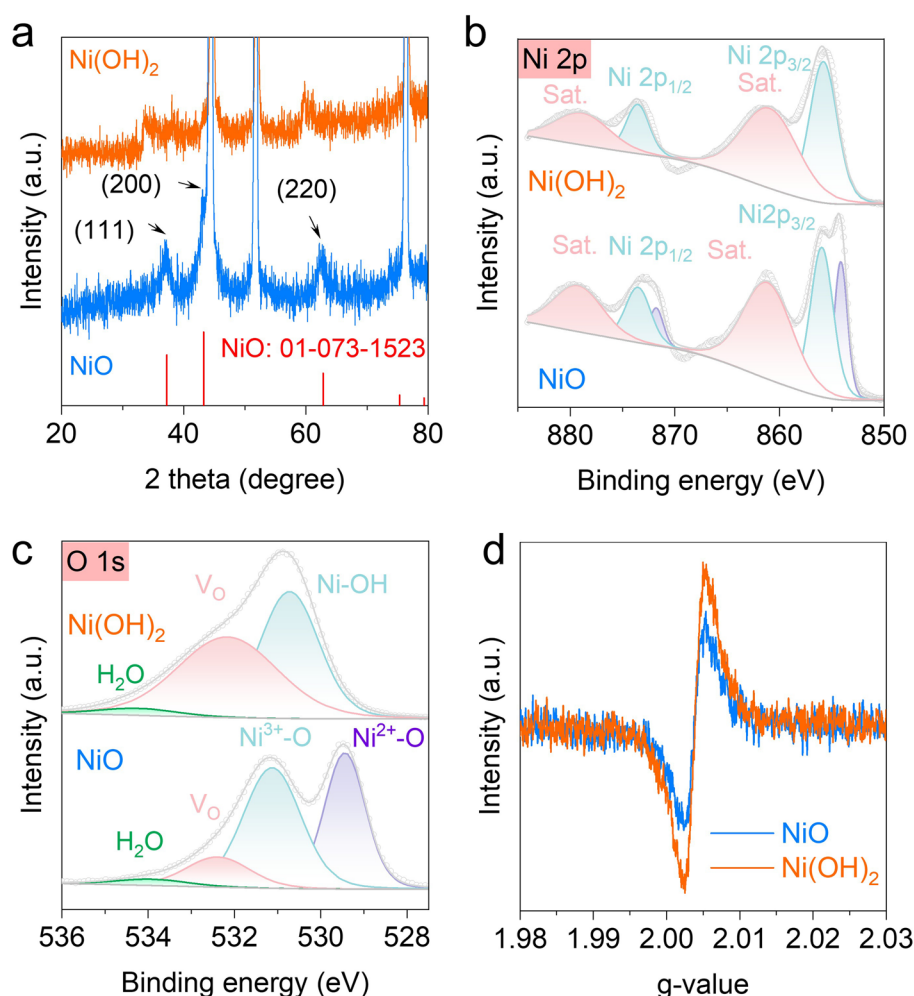


Fig. 1 Structure characterization of Ni(OH)₂ and NiO. **a** XRD patterns of the Ni(OH)₂ and NiO catalysts. High-resolution XPS spectra of **b** Ni 2p and **c** O 1s for Ni(OH)₂ and NiO catalysts. **d** EPR spectra of the Ni(OH)₂ and NiO catalysts

hexahydrate and hexamethylenetetramine in a mixed solution [28]. Then, the $\text{Ni}(\text{OH})_2$ was heated at 300 °C for 3 h under air atmosphere to form nickel oxide (NiO). The XRD pattern (Fig. 1a) shows that the diffraction peaks are indexed to NiO.

The chemistry state of the $\text{Ni}(\text{OH})_2$ and NiO were investigated by X-ray photoelectron spectroscopy (XPS). The high-resolution Ni 2*p* XPS spectra is shown in Fig. 1b. The Ni 2*p* show two major peaks located at 873 and 855 eV, which can be attributed to the Ni 2*p*_{1/2} and Ni 2*p*_{3/2}, respectively. The Ni 2*p*_{3/2} peak of NiO is deconvoluted into two prominent peaks located at 854.1 and 856.0 eV attributed to Ni^{2+} and Ni^{3+} of NiO, respectively [29]. Figure 1c shows the O 1*s* spectra of $\text{Ni}(\text{OH})_2$ and NiO. The peak with the highest intensity at 529.5 eV is assigned to $\text{Ni}^{2+}\text{--O}$ in NiO. The peak at 531.1 eV is related to oxygen-containing species, which is assigned to $\text{Ni}^{3+}\text{--O}$ [29]. The weak peaks at 532.2 and 534 eV belong to oxygen vacancy (V_O) and adsorbed H_2O , respectively [30, 31]. The area of V_O for $\text{Ni}(\text{OH})_2$ is much higher than that of NiO. The electron paramagnetic resonance (EPR) spectrum (Fig. 1d) further confirms the existence of V_O in $\text{Ni}(\text{OH})_2$ and NiO. $\text{Ni}(\text{OH})_2$ shows a

strong EPR signal at around $g=2.003$, indicating rich V_O in $\text{Ni}(\text{OH})_2$ [32], which agrees with the result of XPS. In addition, the Brunauer–Emmett–Teller (BET) specific surface area of NiO and $\text{Ni}(\text{OH})_2$ was tested. As shown in Fig. S2, NiO has a higher specific surface area ($5.67 \text{ m}^2 \text{ g}^{-1}$) than nickel $\text{Ni}(\text{OH})_2$ ($3.49 \text{ m}^2 \text{ g}^{-1}$).

SEM and TEM was used to study the morphology of $\text{Ni}(\text{OH})_2$ and NiO. Figures 2a and S1b–c show that the original $\text{Ni}(\text{OH})_2$ possesses a well-defined 2D nanosheet morphology. After the annealing, the 2D nanosheet morphology is still retained for the NiO samples (Figs. 2d and S1d–e). Figure 2b displays the TEM image of $\text{Ni}(\text{OH})_2$. The inset of Fig. 2b shows the selected area electron diffraction (SAED) pattern of $\text{Ni}(\text{OH})_2$ nanosheet. The pattern shows diffused rings, which means the as-prepared $\text{Ni}(\text{OH})_2$ nanosheet has poor crystallinity. There are no typical lattice fringes from the high-resolution TEM (HRTEM) image of $\text{Ni}(\text{OH})_2$ sample (Fig. 1c), which suggests that the as-prepared $\text{Ni}(\text{OH})_2$ nanosheets are amorphous. Figure S3 shows the high-angle annular dark-field scanning TEM (HAADF-STEM) image and the corresponding EDS elemental mappings of $\text{Ni}(\text{OH})_2$. Ni and O elements were uniformly distributed throughout

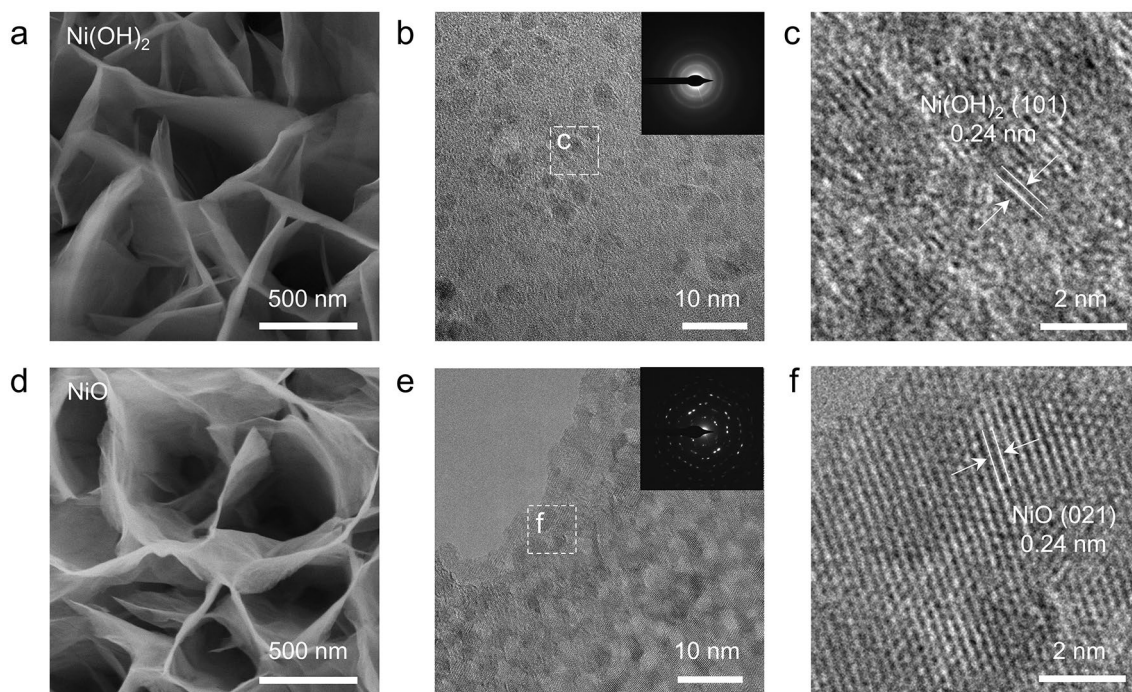


Fig. 2 Morphology characterization of the $\text{Ni}(\text{OH})_2$ and NiO catalysts. **a** SEM, **b** TEM and **c** HRTEM images of $\text{Ni}(\text{OH})_2$, **d** SEM, **e** TEM and **f** HRTEM images of NiO

the nanosheet. The TEM image (Fig. 2e) and SAED pattern (inset of Fig. 2e) of the NiO shows good crystallinity. The HRTEM image of NiO (Fig. 2f) shows the lattice fringes of (021) planes. Figure S4 shows the HAADF-STEM image and the corresponding EDS elemental mappings of NiO.

3.2 Electrocatalytic Performances of Ni(OH)₂ and NiO for GOR

The electrochemical performance of NiO and Ni(OH)₂ was tested in 1.0 M KOH electrolyte with and without 0.1 M glycerol, respectively. Firstly, a typical cyclic voltammetry

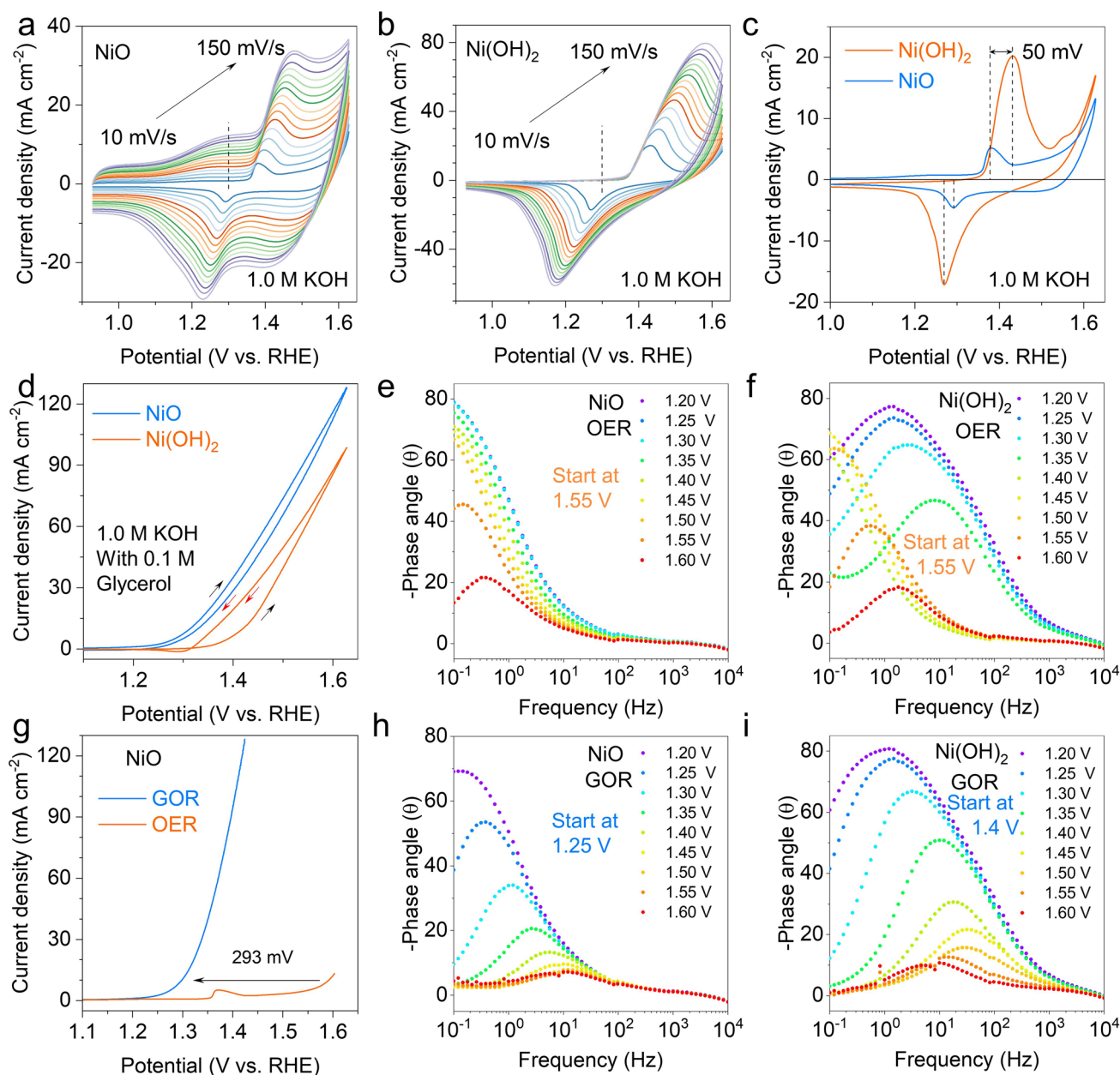


Fig. 3 Electrocatalytic performances of Ni(OH)₂ and NiO for GOR. Cyclic voltammograms of **a** NiO and **b** Ni(OH)₂ electrocatalysts in 1 M KOH at different sweep rates. **c** Comparison of cyclic voltammograms of NiO and Ni(OH)₂ in 1.0 M KOH at 10 mV s⁻¹. **d** CV curves of NiO and Ni(OH)₂ for GOR. **e** LSV curves of NiO for GOR and OER. Bode plots for the **e** NiO and **f** Ni(OH)₂ in 1 M KOH. Bode plots for the **h** NiO and **i** Ni(OH)₂ in 1 M KOH with 0.1 M glycerol

(CV) cycling was carried out in 1 M KOH medium. Figure 3a, b shows the CV curves of NiO and Ni(OH)₂ electrodes at various scan rates, respectively. When the scan rate goes up, the oxidation peak moves to more positive potential, and the reduction peak moves to a more negative potential. Generally, the proton diffusion rate determines the speed of the oxidation of Ni(OH)₂ to NiOOH [33]. The peak current densities were plotted against the square roots of the scan rates in Fig. S5 and a linear relationship was found, Ni(OH)₂ shows higher proton diffusion coefficient than NiO. In addition, it is found that the current density of NiO between 1.0 and 1.35 V increases with the increase of scan rate (Fig. 3a), but this phenomenon is not observed in Ni(OH)₂ (Fig. 3b). Which means that the NiO surface has better adsorption for OH species [21]. Figure 3c shows the CV curves of NiO and Ni(OH)₂ at 5 mV s⁻¹, where the Ni oxidation peak potential for NiO is lower than that for Ni(OH)₂, indicating that NiO is easier to be oxidized.

The electrocatalytic performance of NiO and Ni(OH)₂ towards the GOR was tested in an electrolyte of 1 M KOH containing 0.1 M glycerol. From the CV curves in Fig. 3d, NiO has the lower onset potential than Ni(OH)₂, showing better electrochemical performance. A CV method was used to measure the electrochemical double-layer capacitance (C_{dl}) of the catalysts and evaluate their electrochemically surface area (ECSA) from C_{dl} (Fig. S6) in order to better understand the improvement of the GOR activity. The results show that NiO has a considerably larger C_{dl} (12.3 mF cm⁻²) than Ni(OH)₂ (0.79 mF cm⁻²). From the linear sweep voltammetry (LSV) curve with IR correction (Fig. 3g), it can be seen that the addition of glycerol to the KOH electrolyte significantly reduces the reaction potential at the anode (293 mV). This suggests that the operating potential during hydrogen production from electrolytic water is expected to be reduced by replacing the OER with GOR. Inspired by this, OER can be replaced by GOR to reduce the potential of hydrogen production by water electrolysis, and at the same time, high value-added formate can be produced at the anode [20]. Compared with other reported transition metal catalysts, NiO exhibits better GOR performance (Table S1). We also compared the electrocatalytic oxidation performance of NiO and Ni(OH)₂ in 1 M KOH containing 0.1 M other alcohols (including ethylene glycol, ethanol, methanol), as shown in Fig. S7. It can be seen that for the ethylene glycol oxidation reaction (EGOR, Fig. S7a), the oxidation potential of NiO is lower than that of Ni(OH)₂; in the ethanol

oxidation reaction (EtOR, Fig. S7b), there is no significant difference; in the methanol oxidation reaction (MOR, Fig. S7e), Ni(OH)₂ is better than NiO. Overall, NiO seems to have a differential ability to oxidize different alcohols (Fig. S7c).

The difference of electrochemical activity between NiO and Ni(OH)₂ were further studied by the in-situ EIS during the OER and GOR (Figs. 3e, f, h, i and S8). From the Bode phase plots, Ni(OH)₂ has a peak in the low-frequency (10⁰–10¹ Hz) region between 1.2 and 1.35 V during the OER (Fig. 3f), which may be related to the formation of oxide species on the electrode surface [22]. But this phenomenon is not observed in NiO (Fig. 3e). When the potential is increased to 1.55 V, new peaks (about 10⁻¹–10⁰ Hz) appear in both NiO and Ni(OH)₂, which may be associated with the start of the OER. After adding 0.1 M glycerol into the KOH, a peak conversion was examined at the potential of 1.25 V for NiO (Fig. 3h) and 1.4 V and Ni(OH)₂ (Fig. 3i), respectively, for GOR. Furthermore, in the Nyquist plots (Fig. S8), the charge-transfer resistance of NiO is much smaller than that of Ni(OH)₂. The EIS analysis shows that the lower charge-transfer resistance of NiO accelerates the kinetics of GOR.

Further, a chronopotentiometric measurement was used to test the stability of NiO for GOR (Fig. S9). As the oxidation reaction continues, glycerol is gradually consumed and the potential decreases. The XPS of NiO and Ni(OH)₂ after the GOR was also tested, as shown in the Figs. S10 and S11. The oxidation peak area of Ni in NiO increases after GOR (Fig. S10a). In addition, a new C=O peak is observed in the C 1s spectrum (Fig. S10c), indicating the existence of residual formate. From the SEM image in Fig. S12, it can be seen that after GOR, NiO still maintains its 3D nanosheet stacked structure without significant changes. And there is also no significant change in the XRD pattern (Fig. S13).

3.3 Characterization of the NiMoNH HER Catalysts

To couple the anodic GOR, a nickel-molybdenum-based catalyst for cathodic HER is also developed, which is a very promising non-precious metal electrocatalyst. Firstly, NiMoO nanoarrays were grown on NF matrix by a hydrothermal method, and then highly active hydrogen evolution catalyst (denoted as NiMoNH) was obtained by annealing in NH₃ and Ar/H₂ atmosphere (Fig. S14). SEM images



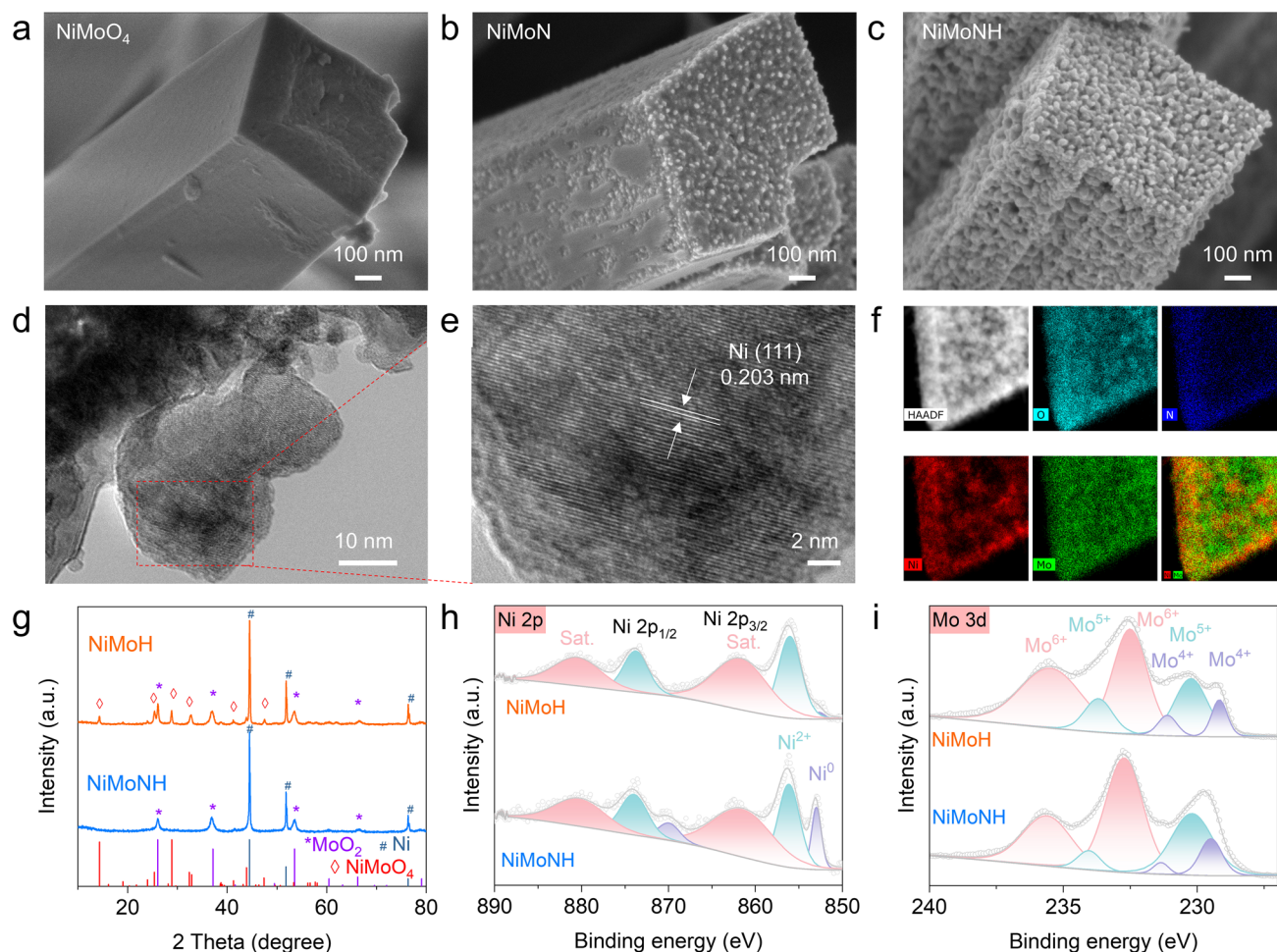


Fig. 4 Characterization of the NiMoNH HER catalysts. SEM images of **a** NiMoO₄, **b** NiMoN and **c** NiMoNH. **d** TEM image, **e** HRTEM image, **f** HADDF-STEM and EDS mapping images of NiMoNH. **g** XRD pattern, **h** Ni 2p XPS spectra and **i** Mo 3p XPS spectra of NiMoH and NiMoNH

(Figs. 4a–c and S14) show the morphology change from NiMoO₄ to NiMoNH. In Fig. 4a and S14b–c, it is noted that NiMoO₄ display nanopillar array and relatively smooth surface. After annealing in NH₃ atmosphere, some nanoparticles appeared on the surface and became rough (Figs. 4b and S14e–f). Finally, after further calcination in an Ar/H₂ atmosphere, the surface of NiMoNH nanopillars are covered with nanoparticles and become extremely rough (Figs. 4c and S14h–i). The unique 3D nanoarray structure will facilitate the release of hydrogen [34, 35]. In addition, the sample annealed directly in argon–hydrogen atmosphere was also synthesized as a control sample (note as NiMoH). The particle size on its surface is slightly larger than that of NiMoNH (Fig. S15).

TEM images further reveal the microstructure of NiMoNH (Figs. 4d and S16). From the HRTEM image (Fig. 4e), the NiMoNH nanoparticles show the lattice fringes of 0.203 nm, which is related to the (111) plane of Ni. Aggregation of Ni particles is also verified in the HADDF-STEM image with the corresponding EDS mappings (Fig. 4f). XRD pattern in Fig. 4g reveals that NiMoNH consists of MoO₂ and Ni phases. While the NiMoO₄ phase can still be found in NiMoH, which indicates incomplete conversion of NiMoO₄.

The chemical states of NiMoNH and NiMoH were further analyzed by XPS. As shown in Fig. 4h, the high-resolution Ni 2p_{3/2} XPS spectra of NiMoNH exhibit a clear intensity increase at ~853 eV, which proves the existence of metal

Ni (0). The high-resolution Mo 3*d* signal of NiMONH and NiMoH (Fig. 4i) were fitted into three typical components at 229.2, 230.4, and 232.2 eV, corresponding to Mo⁴⁺, Mo⁵⁺, and Mo⁶⁺, respectively [36]. In the N 1*s* XPS spectrum of

NiMoNH (Fig. S17), there is a peak at 397.4 eV that corresponds to the N species in metal nitrides, and another peak at 399.6 eV that is due to the incomplete reaction of NH₃ [37].

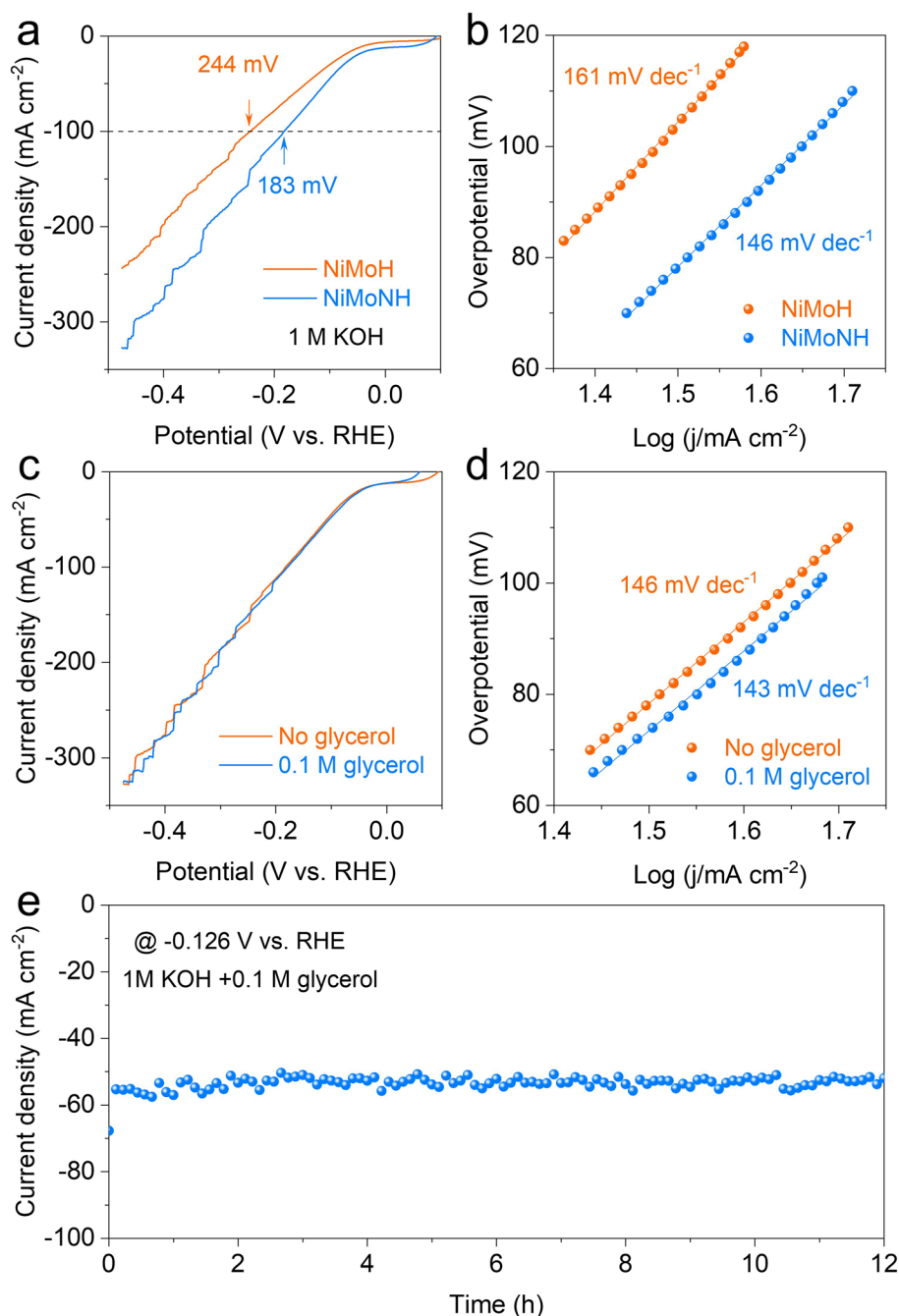


Fig. 5 HER performance of NiMoNH. **a** LSV curves and **b** the corresponding Tafel plots of NiMoNH and NiMoH in 1.0 M KOH. **c** LSV curves and **d** the corresponding Tafel plots of NiMoNH in 1.0 M KOH with and without 0.1 M glycerol. **e** Chronoamperometry curves (i-t) recorded on NiMoNH for HER at -0.126 V vs. RHE



3.4 HER Performance of NiMoNH

The HER performance of NiMoNH and NiMoH on Ni foam was tested in 1 M KOH. In Fig. 5a, the LSV curves show that NiMoNH exhibited the better catalytic activity than NiMoH. The overpotential requirements at current densities of 100 mA cm^{-2} were ~ 183 and 224 mV for the NiMoNH and NiMoH, respectively. NiMoNH and NiMoH exhibit the Tafel slope (Fig. 5b) of 146 and 161 mV dec^{-1} , respectively. The HER performance of NiMoNH catalyst in 1 M KOH containing 0.1 M glycerol was further examined. Excitingly, the addition of glycerol has no obvious effect on the HER performance of NiMoNH (Fig. 5c), which is extremely important for the subsequent development of GOR-assisted hydrogen production. As shown in Fig. 5d, NiMoNH shows the similar Tafel slopes in different electrolyte medium, which means that it has similar catalytic kinetics. Compared

with other NiMo-based catalysts (Table S2), NiMoNH has similar HER performance. In addition, the stability of NiMoNH was also tested as shown in Fig. 5e. NiMoNH can perform stably at -0.126 V vs. RHE for 12 h and is potential to be used as a cathode for electrolyzer. SEM images (Fig. S18) and XRD pattern (Fig. S19) of NiMoNH after stability testing showed no significant changes in the morphology and structure of the material, with good stability.

3.5 Performance of Hybrid Electrolyzer

Considering that the as-synthesized NiO and NiMoNH have excellent GOR and HER properties, respectively. A H-type electrolyzer with membrane was used to test their hybrid electrolysis performance. Figure 6a shows that the LSV curves of the electrolyzer with and without glycerol. The anion exchange membrane (AEM) flow cell represented

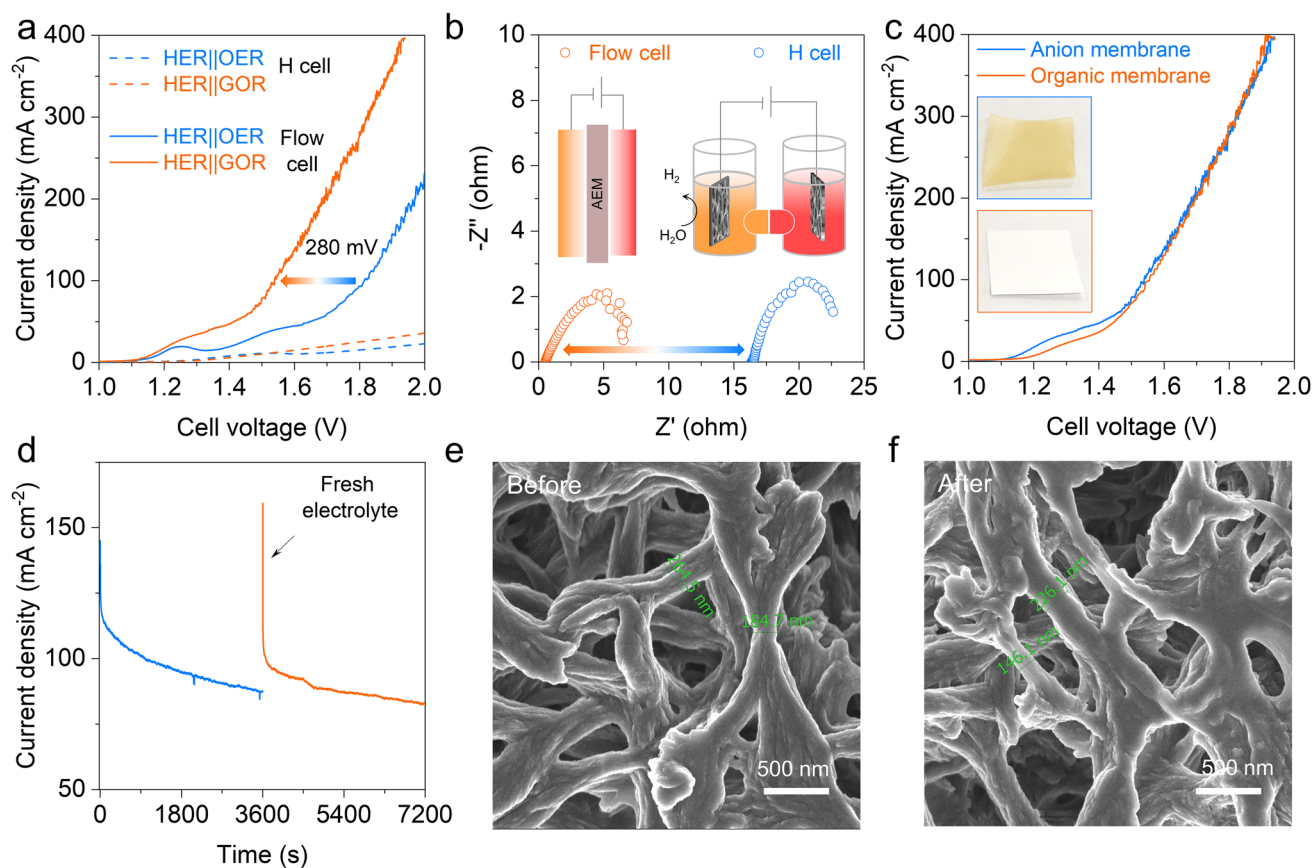


Fig. 6 Performance of hybrid electrolyzer (using NiO/NF as anodic electrocatalyst and NiMoNH/NF as cathodic electrocatalyst). **a** Polarization curve of the hybrid electrolyzer. **b** Nyquist plots from the EIS measurements for MEA cell and H cell. **c** Polarization curve of the hybrid electrolyzer with alkaline anion membrane and organic membrane. **d** Chronoamperometry curve of the hybrid electrolyzer using organic membrane at 1.6 V . SEM images of organic membrane **e** before and **f** after long-term testing

by the solid line exhibits a higher current density than the H-type cell (dash line). The GOR-assisted hydrogen production (HER||GOR) only requires a cell voltage of 1.54 V at a current density of 100 mA cm^{-2} , which is remarkably reduced by 280 mV compared to the overall water splitting (HER||OER). The advantage of the flow cell was further confirmed by electrochemical impedance spectroscopy (EIS) analysis (Fig. 6b). It can be seen from the Nyquist plots that the contact resistance of the flow cell is much smaller than that of H cell.

Considering that the anode OER is replaced by GOR, this process has no oxygen generation and cannot induce explosive H_2/O_2 mixtures. Therefore, a cheaper organic filter membrane (Nylon) was used to replace the expensive AEM (inset of Fig. 6c). The NiMoNH cathode, organic membrane and NiO anode were assembled in the flow cell. The pores of the organic membrane allow the free transport of K^+ and OH^- , while the physical isolation of cathode and anode is realized. As shown in Fig. 6c, the replacement of the membrane has not induced degradation of the electrochemical performance. Compared to other small molecule oxidation assisted hydrogen production devices (Table S3), the electrolyzer potential assembled in this work is lower. Moreover, the assembled flow cell also exhibits good stability (Fig. 6d), where the drop in current is associated with the depletion of glycerol molecule. The morphology of the organic member before and after stability test of the flow cell were investigated by SEM. As shown in Fig. 6d, the organic membrane has abundant pores for ion transport and mass transfer. No obvious change is observed after the stability test (Fig. 6f), which indicates that the organic membrane is feasible to be used in HER||GOR system at low cost for long-term operation.

4 Conclusions

In summary, vertical 3D NiO nanoflakes and NiMoNH nanopillars have been successfully synthesized to use as electrocatalysts for the anodic GOR and cathodic HER, respectively. The replacement of OER with GOR together with the highly active NiO nanoflakes remarkably reduces the operation voltage of electrolyzer for hydrogen evolution. Furthermore, cheaper organic membrane instead of an anion exchange membrane is employed as separator to lower the

whole cost of electrolyzer. The as-assembled electrolyzer exhibits good HER performance and long-term stability. This work opens a new avenue for the practical applications in the future hydrogen economy.

Acknowledgements The authors are grateful to the financial support from National Natural Science Foundation of China (92163117, 52072389, 52172058, 51972006).

Funding Open access funding provided by Shanghai Jiao Tong University.

Declarations

Conflict of interest The authors declare no interest conflict. They have no known competing financial interests or personal relationships that could have appeared to influence the work reported in this paper.

Open Access This article is licensed under a Creative Commons Attribution 4.0 International License, which permits use, sharing, adaptation, distribution and reproduction in any medium or format, as long as you give appropriate credit to the original author(s) and the source, provide a link to the Creative Commons licence, and indicate if changes were made. The images or other third party material in this article are included in the article's Creative Commons licence, unless indicated otherwise in a credit line to the material. If material is not included in the article's Creative Commons licence and your intended use is not permitted by statutory regulation or exceeds the permitted use, you will need to obtain permission directly from the copyright holder. To view a copy of this licence, visit <http://creativecommons.org/licenses/by/4.0/>.

Supplementary Information The online version contains supplementary material available at <https://doi.org/10.1007/s40820-023-01150-1>.

References

1. B. Guo, Y. Ding, H. Huo, X. Wen, X. Ren et al., Recent advances of transition metal basic salts for electrocatalytic oxygen evolution reaction and overall water electrolysis. *Nano-Micro Lett.* **15**(1), 57 (2023). <https://doi.org/10.1007/s40820-023-01038-0>
2. C. Wang, Q. Zhang, B. Yan, B. You, J. Zheng et al., Facet engineering of advanced electrocatalysts toward hydrogen/oxygen evolution reactions. *Nano-Micro Lett.* **15**(1), 52 (2023). <https://doi.org/10.1007/s40820-023-01024-6>
3. Z. Wang, Z. Lin, Y. Wang, S. Shen, Q. Zhang et al., Nontrivial topological surface states in Ru_3Sn_7 toward wide ph-range hydrogen evolution reaction. *Adv. Mater.* **35**(25), e2302007 (2023). <https://doi.org/10.1002/adma.202302007>
4. X. Wang, J. Zhang, Z. Wang, Z. Lin, S. Shen et al., Fabricating Ru single atoms and clusters on cop for boosted hydrogen



- evolution reaction. *Chin. J. Struct. Chem.* **42**(4), 100035 (2023). <https://doi.org/10.1016/j.cjsc.2023.100035>
5. S. Li, Z. Li, R. Ma, C. Gao, L. Liu et al., A glass-ceramic with accelerated surface reconstruction toward the efficient oxygen evolution reaction. *Angew. Chem. Int. Ed.* **60**(7), 3773–3780 (2021). <https://doi.org/10.1002/anie.202014210>
 6. Y. Li, X. Wei, L. Chen, J. Shi, Electrocatalytic hydrogen production trilogy. *Angew. Chem. Int. Ed.* **60**(36), 19550–19571 (2021). <https://doi.org/10.1002/anie.202009854>
 7. D. Yan, C. Mebrahtu, S. Wang, R. Palkovits, Innovative electrochemical strategies for hydrogen production: from electricity input to electricity output. *Angew. Chem. Int. Ed.* **62**(16), e202214333 (2023). <https://doi.org/10.1002/anie.202214333>
 8. H. Liu, N. Agrawal, A. Ganguly, Y. Chen, J. Lee et al., Ultra-low voltage bipolar hydrogen production from biomass-derived aldehydes and water in membrane-less electrolyzers. *Energy Environ. Sci.* **15**(10), 4175–4189 (2022). <https://doi.org/10.1039/d2ee01427k>
 9. J. Du, D. Xiang, K. Zhou, L. Wang, J. Yu et al., Electrochemical hydrogen production coupled with oxygen evolution, organic synthesis, and waste reforming. *Nano Energy* **104**, 107875 (2022). <https://doi.org/10.1016/j.nanoen.2022.107875>
 10. B. Rausch, M.D. Symes, G. Chisholm, L. Cronin, Decoupled catalytic hydrogen evolution from a molecular metal oxide redox mediator in water splitting. *Science* **345**(6202), 1326–1330 (2014). <https://doi.org/10.1126/science.1257443>
 11. B. You, Y. Sun, Innovative strategies for electrocatalytic water splitting. *Acc. Chem. Res.* **51**(7), 1571–1580 (2018). <https://doi.org/10.1021/acs.accounts.8b00002>
 12. H. Jin, X. Wang, C. Tang, A. Vasileff, L. Li et al., Stable and highly efficient hydrogen evolution from seawater enabled by an unsaturated nickel surface nitride. *Adv. Mater.* **33**(13), e2007508 (2021). <https://doi.org/10.1002/adma.202007508>
 13. F. Sun, J. Qin, Z. Wang, M. Yu, X. Wu et al., Energy-saving hydrogen production by chlorine-free hybrid seawater splitting coupling hydrazine degradation. *Nat. Commun.* **12**(1), 4182 (2021). <https://doi.org/10.1038/s41467-021-24529-3>
 14. S.-K. Geng, Y. Zheng, S.-Q. Li, H. Su, X. Zhao et al., Nickel ferrocyanide as a high-performance urea oxidation electrocatalyst. *Nat. Energy* **6**(9), 904–912 (2021). <https://doi.org/10.1038/s41560-021-00899-2>
 15. W. Chen, L. Xu, X. Zhu, Y.C. Huang, W. Zhou et al., Unveiling the electrooxidation of urea: intramolecular coupling of the N-N bond. *Angew. Chem. Int. Ed.* **60**(13), 7297–7307 (2021). <https://doi.org/10.1002/anie.202015773>
 16. S. Li, R. Ma, J. Hu, Z. Li, L. Liu et al., Coordination environment tuning of nickel sites by oxyanions to optimize methanol electro-oxidation activity. *Nat. Commun.* **13**(1), 2916 (2022). <https://doi.org/10.1038/s41467-022-30670-4>
 17. B. Zhao, J. Liu, X. Wang, C. Xu, P. Sui et al., CO₂-emission-free electrocatalytic CH₃OH selective upgrading with high productivity at large current densities for energy saved hydrogen co-generation. *Nano Energy* **80**, 105530 (2021). <https://doi.org/10.1016/j.nanoen.2020.105530>
 18. F. Meng, C. Dai, Z. Liu, S. Luo, J. Ge et al., Methanol electro-oxidation to formate on iron-substituted lanthanum cobaltite perovskite oxides. *eScience* **2**(1), 87–94 (2022). <https://doi.org/10.1016/j.esci.2022.02.001>
 19. J. Hao, J. Liu, D. Wu, M. Chen, Y. Liang et al., In situ facile fabrication of Ni(OH)₂ nanosheet arrays for electrocatalytic co-production of formate and hydrogen from methanol in alkaline solution. *Appl. Catal. B* **281**, 119510 (2021). <https://doi.org/10.1016/j.apcatb.2020.119510>
 20. Y. Li, X. Wei, L. Chen, J. Shi, M. He, Nickel-molybdenum nitride nanoplate electrocatalysts for concurrent electrolytic hydrogen and formate productions. *Nat. Commun.* **10**(1), 5335 (2019). <https://doi.org/10.1038/s41467-019-13375-z>
 21. S. Li, P. Ma, C. Gao, L. Liu, X. Wang et al., Reconstruction-induced NiCu-based catalysts towards paired electrochemical refining. *Energy Environ. Sci.* **15**(7), 3004–3014 (2022). <https://doi.org/10.1039/d2ee00461e>
 22. Y. Lu, C.L. Dong, Y.C. Huang, Y. Zou, Z. Liu et al., Identifying the geometric site dependence of spinel oxides for the electrooxidation of 5-hydroxymethylfurfural. *Angew. Chem. Int. Ed.* **59**(43), 19215–19221 (2020). <https://doi.org/10.1002/anie.202007767>
 23. N. Zhang, Y. Zou, L. Tao, W. Chen, L. Zhou et al., Electrochemical oxidation of 5-hydroxymethylfurfural on nickel nitride/carbon nanosheets: reaction pathway determined by in situ sum frequency generation vibrational spectroscopy. *Angew. Chem. Int. Ed.* **58**(44), 15895–15903 (2019). <https://doi.org/10.1002/anie.201908722>
 24. T. Wang, L. Tao, X. Zhu, C. Chen, W. Chen et al., Combined anodic and cathodic hydrogen production from aldehyde oxidation and hydrogen evolution reaction. *Nat. Catal.* **5**(1), 66–73 (2021). <https://doi.org/10.1038/s41929-021-00721-y>
 25. W.J. Liu, Z. Xu, D. Zhao, X.Q. Pan, H.C. Li et al., Efficient electrochemical production of glucaric acid and H₂ via glucose electrolysis. *Nat. Commun.* **11**(1), 265 (2020). <https://doi.org/10.1038/s41467-019-14157-3>
 26. Y. Zhang, B. Zhou, Z. Wei, W. Zhou, D. Wang et al., Coupling glucose-assisted Cu(I)/Cu(II) redox with electrochemical hydrogen production. *Adv. Mater.* **33**(48), e2104791 (2021). <https://doi.org/10.1002/adma.202104791>
 27. J.F. Gomes, G. Tremiliosi-Filho, Spectroscopic studies of the glycerol electro-oxidation on polycrystalline Au and Pt surfaces in acidic and alkaline media. *Electrocatalysis* **2**(2), 96–105 (2011). <https://doi.org/10.1007/s12678-011-0039-0>
 28. D. Liu, L. Cao, Z. Luo, D. Zhong, J. Tan et al., An in situ generated amorphous CoFePi and crystalline Ni(PO₃)₂ heterojunction as an efficient electrocatalyst for oxygen evolution. *J. Mater. Chem. A* **6**(48), 24920–24927 (2018). <https://doi.org/10.1039/c8ta10378j>
 29. P. Yang, L. Li, S. Yu, H. Zheng, W. Peng, The annealing temperature and films thickness effect on the surface morphology, preferential orientation and dielectric property of NiO films. *Appl. Surf. Sci.* **493**, 396–403 (2019). <https://doi.org/10.1016/j.apsusc.2019.06.223>
 30. W. Wang, Y. Wang, R. Yang, Q. Wen, Y. Liu et al., Vacancy-rich Ni(OH)₂ drives the electrooxidation of amino C-N

- bonds to nitrile $C\equiv N$ bonds. *Angew. Chem. Int. Ed.* **59**(39), 16974–16981 (2020). <https://doi.org/10.1002/anie.202005574>
31. W. Yang, X. Yang, J. Jia, C. Hou, H. Gao et al., Oxygen vacancies confined in ultrathin nickel oxide nanosheets for enhanced electrocatalytic methanol oxidation. *Appl. Catal. B* **244**, 1096–1102 (2019). <https://doi.org/10.1016/j.apcatb.2018.12.038>
32. J. Balamurugan, T.T. Nguyen, V. Aravindan, N.H. Kim, J.H. Lee, Highly reversible water splitting cell building from hierarchical 3d nickel manganese oxyphosphide nanosheets. *Nano Energy* **69**, 104432 (2020). <https://doi.org/10.1016/j.nanoen.2019.104432>
33. J. Li, Z. Luo, Y. Zuo, J. Liu, T. Zhang et al., NiSn bimetallic nanoparticles as stable electrocatalysts for methanol oxidation reaction. *Appl. Catal. B* **234**, 10–18 (2018). <https://doi.org/10.1016/j.apcatb.2018.04.017>
34. X. Yu, Z.Y. Yu, X.L. Zhang, Y.R. Zheng, Y. Duan et al., “Superaerophobic” nickel phosphide nanoarray catalyst for efficient hydrogen evolution at ultrahigh current densities. *J. Am. Chem. Soc.* **141**(18), 7537–7543 (2019). <https://doi.org/10.1021/jacs.9b02527>
35. Z. Wang, J. Chen, E. Song, N. Wang, J. Dong et al., Manipulation on active electronic states of metastable phase β -NiMoO₄ for large current density hydrogen evolution. *Nat. Commun.* **12**(1), 5960 (2021). <https://doi.org/10.1038/s41467-021-26256-1>
36. Y.Y. Chen, Y. Zhang, X. Zhang, T. Tang, H. Luo et al., Self-templated fabrication of MoNi₄/MoO_{3-x} nanorod arrays with dual active components for highly efficient hydrogen evolution. *Adv. Mater.* **29**(39), 1703311 (2017). <https://doi.org/10.1002/adma.201703311>
37. L. Yu, Q. Zhu, S. Song, B. McElhenny, D. Wang et al., Non-noble metal-nitride based electrocatalysts for high-performance alkaline seawater electrolysis. *Nat. Commun.* **10**(1), 5106 (2019). <https://doi.org/10.1038/s41467-019-13092-7>

